6th European Conference on Computational Mechanics (ECCM 6)
7th European Conference on Computational Fluid Dynamics (ECFD 7)
11-15 June 2018, Glasgow, UK

STATE-OF-THE-ART FINITE-VOLUME DISCRETISATION OF KAPILA'S TWO-FLUID FLOW MODEL

R. de Böck[1], A.S. Tijsseling[2] and B. Koren[3]

Eindhoven University of Technology, Centre for Analysis, Scientific Computing and Applications
P.O. Box 513, 5600 MB Eindhoven, The Netherlands,
[1] r.d.bock@tue.nl,[2] a.s.tijsseling@tue.nl,[3] b.koren@tue.nl

Key words: Two-fluid flow model, Finite-volume method, Limiters

Abstract. In preparation of the study of liquefied natural gas (LNG) sloshing in ships and vehicles, we model and numerically analyse compressible two-fluid flow. We consider a five-equation two-fluid flow model, assuming velocity and pressure continuity across two-fluid interfaces, with a separate equation to track the interfaces. The system of partial differential equations is hyperbolic and quasi-conservative. It is discretised in space with a tailor-made third-order accurate finite-volume method, employing an HLLC approximate Riemann solver. The third-order accuracy is obtained through spatial reconstruction with a limiter function, for which a novel formulation is presented. The non-homogeneous term is handled in a way consistent with the HLLC method. We study the one-dimensional case of a liquid column impacting onto a gas pocket entrapped at a solid wall. It mimics the impact of a breaking wave in an LNG containment system, where a gas pocket is entrapped at the tank wall below the wave crest. Furthermore, the impact of a shock wave on a gas bubble containing the heavy gas R22, immersed in air, is simulated and compared with experimental results. The computational results are consistent with the experimental results.

1 Introduction

In this paper we study a model that describes the flow of two fluids. Both fluids are assumed to be compressible, inviscid and non-heat-conducting. Furthermore, no chemical reactions or phase changes occur. Analysis of this type of fluid flow has various industrial applications, including sloshing inside LNG tanks [4].

Five-equation models are obtained by assuming velocity and pressure equilibrium across the material interfaces. We use the Kapila model [9]. Another, equivalent formulation has also been proposed [20, 11]. We apply a finite-volume method to the system, ensuring the global numerical conservation of mass, momentum and energy. At each finite-volume interface we apply the HLLC approximate Riemann solver to calculate the fluxes [19]. In the exact two-fluid flow formulation we may have a sharp material interface, which is seriously diffused when applying a first-order accurate numerical scheme. Therefore, we employ higher-order spatial reconstruction to the finite-volume method, using the MUSCL approach [12]. To prevent spurious oscillations a limiter is used. We introduce a new limiter and compare it to some standard ones.

2 Mathematical model

A well-known two-fluid flow model is the Baer-Nunziato seven-equation model [1]. It consists of two systems of conservation laws, one for each of the two fluids. To complete the model, another equation, describing the presence and proportion of each of the two fluids, is required: the equation for the volume fraction. The Kapila model is a reduced form of the Baer-Nunziato model. Kapila et al. [9] argue that for many applications the time scale of equilibration of both velocity and pressure differences across material interfaces is sufficiently small to assume thermodynamic equilibrium. This allows the model to be reduced to one consisting of five equations: four conservation laws (two for mass, one for energy and a vector equation for momentum), and a non-conservative equation for the volume fraction of one of the fluids. The latter contains a non-conservative term due to energy exchange between the fluids. The *volume fraction* α is defined as the fraction of a control volume which is occupied by fluid 1. It takes the value 1 at a point in space and time $(\mathbf{x}, t)$ if $(\mathbf{x}, t)$ is located fully within fluid 1, and 0 when it is fully within fluid 2. At the two-fluid interface α takes intermediate values, leading to a diffused interface. The density ρ, specific total energy E and specific internal energy e are decomposed using the volume fraction α:

$$\rho = \alpha\rho_1 + (1-\alpha)\rho_2, \quad E = E_1\alpha\rho_1/\rho + E_2(1-\alpha)\rho_2/\rho, \quad e = e_1\alpha\rho_1/\rho + e_2(1-\alpha)\rho_2/\rho. \tag{1}$$

Because of the pressure and velocity equilibrium across two-fluid interfaces, considering two spatial dimensions, we assume

$$p = p_1 = p_2, \quad u = u_1 = u_2, \quad v = v_1 = v_2, \tag{2}$$

with p the pressure and u and v the velocity components in the x- and y-direction, respectively. The Kapila system in two dimensions is given by

$$\frac{\partial}{\partial t}\mathbf{q} + \frac{\partial}{\partial x}\mathbf{f} + \frac{\partial}{\partial y}\mathbf{g} = \mathbf{s}, \tag{3}$$

$$\mathbf{q} = \begin{bmatrix} \rho \\ \rho u \\ \rho v \\ \rho E \\ \rho\beta \\ \alpha \end{bmatrix}, \quad \mathbf{f} = \begin{bmatrix} \rho u \\ \rho u^2 + p \\ \rho uv \\ u(\rho E + p) \\ \alpha\rho_1 u \\ \alpha u \end{bmatrix}, \quad \mathbf{g} = \begin{bmatrix} \rho v \\ \rho uv \\ \rho v^2 + p \\ v(\rho E + p) \\ \alpha\rho_1 v \\ \alpha v \end{bmatrix}, \quad \mathbf{s} = \begin{bmatrix} 0 \\ 0 \\ 0 \\ 0 \\ 0 \\ (\alpha - \phi)(u_x + v_y) \end{bmatrix}. \tag{4}$$

Here $\phi := \alpha(1-\alpha)\frac{\rho_1 c_1^2 - \rho_2 c_2^2}{(1-\alpha)\rho_1 c_1^2 + \alpha\rho_2 c_2^2}$ is a parameter depending on the compressibilities of the fluids, and c_i is the speed of sound in fluid i. This system needs to be closed with an equation of state (EOS) for each of the fluids, relating the pressure, density and internal energy. Here we will consider the perfect gas EOS, and the stiffened gas EOS, respectively:

$$e_i = \frac{p}{\rho_i(\gamma_i - 1)}, \quad e_i = \frac{p + \pi_i\gamma_i}{\rho_i(\gamma_i - 1)}, \tag{5}$$

where γ_i is the ratio of specific heats, which is a material constant, and π_i is another material constant needed to describe liquids.

2.1 The Kapila system of equations

The system (3) can be expressed in primitive variables $\rho, u, v, p, \alpha, \beta$, resulting in,

$$\frac{\partial}{\partial t}\mathbf{w} + \mathbf{A}\frac{\partial \mathbf{w}}{\partial x} + \mathbf{B}\frac{\partial \mathbf{w}}{\partial y} = \mathbf{0}, \tag{6}$$

$$\mathbf{w} = \begin{bmatrix} \rho \\ u \\ v \\ p \\ \alpha \\ \beta \end{bmatrix}, \quad \mathbf{A} = \begin{bmatrix} u & \rho & 0 & 0 & 0 & 0 \\ 0 & u & 0 & \frac{1}{\rho} & 0 & 0 \\ 0 & 0 & u & 0 & 0 & 0 \\ 0 & \rho c^2 & 0 & u & 0 & 0 \\ 0 & \phi & 0 & 0 & u & 0 \\ 0 & 0 & 0 & 0 & 0 & u \end{bmatrix}, \quad \mathbf{B} = \begin{bmatrix} v & 0 & \rho & 0 & 0 & 0 \\ 0 & v & 0 & 0 & 0 & 0 \\ 0 & 0 & v & \frac{1}{\rho} & 0 & 0 \\ 0 & 0 & \rho c^2 & v & 0 & 0 \\ 0 & 0 & \phi & 0 & v & 0 \\ 0 & 0 & 0 & 0 & 0 & v \end{bmatrix}. \tag{7}$$

Here, c is the speed of sound of the mixture, obtained from Wood's relation [21]:

$$\frac{1}{\rho c^2} = \frac{\alpha}{\rho_1 c_1^2} + \frac{1-\alpha}{\rho_2 c_2^2}. \tag{8}$$

The eigenvalues of $\mathbf{A}$ and $\mathbf{B}$ are $u-c, u, u+c$ and $v-c, v, v+c$, respectively, where the eigenvalues u and v are both quadruple. The eigenvalues are all real-valued, making the system hyperbolic.

3 Numerical approach

We consider the Kapila system (3) in integral form, at some point in time, say t:

$$\frac{\partial}{\partial t}\int_\Omega \mathbf{q}\mathrm{d}\Omega + \oint_\Gamma [\mathbf{f}, \mathbf{g}]\cdot \mathbf{n}\mathrm{d}\Gamma = \int_\Omega \mathbf{s}\mathrm{d}\Omega, \tag{9}$$

with Ω a control volume and Γ its boundary. We divide the computational domain into equal rectangular cells with width Δx and length Δy, average state $\mathbf{q}_{i,j}$ and average source term $\mathbf{s}_{i,j}$. In semi-discrete form we then have

$$\frac{d}{dt}\mathbf{q}_{i,j} = -\frac{1}{\Delta x}\left(\mathbf{f}_{i+\frac{1}{2},j} - \mathbf{f}_{i-\frac{1}{2},j}\right) - \frac{1}{\Delta y}\left(\mathbf{g}_{i,j+\frac{1}{2}} - \mathbf{g}_{i,j-\frac{1}{2}}\right) + \mathbf{s}_{i,j}. \tag{10}$$

The basic numerical method for (10) is the first-order accurate Godunov method with forward Euler time integration, yielding:

$$\begin{aligned} \mathbf{q}_{i,j}^{n+1} = \mathbf{q}_{i,j}^n &+ \frac{\Delta t}{\Delta x}\left(\mathbf{F}(\mathbf{q}_{i-1,j}^n, \mathbf{q}_{i,j}^n) - \mathbf{F}(\mathbf{q}_{i,j}^n, \mathbf{q}_{i+1,j}^n)\right) \\ &+ \frac{\Delta t}{\Delta y}\left(\mathbf{G}(\mathbf{q}_{i,j-1}^n, \mathbf{q}_{i,j}^n) - \mathbf{G}(\mathbf{q}_{i,j}^n, \mathbf{q}_{i,j+1}^n)\right) + \Delta t\ \mathbf{s}_{i,j}^n, \end{aligned} \tag{11}$$

with Δt the time step and $\mathbf{F}, \mathbf{G}$ the Riemann fluxes. Both the flux computation and the time integration will be performed in a more accurate manner, as outlined in the following.

3.1 Spatial discretization

To achieve higher-order spatial accuracy we perform spatial reconstruction, known as the MUSCL (Monotone Upstream-centred Scheme for Conservation Laws) approach [12]. We present it here for the one-dimensional case. The formulation is easily extended to two- and three-dimensional cases, treating the fluxes in each of the separate directions in a locally one-dimensional fashion. To make the scheme monotone we apply a slope limiter φ to the primitive variables $\mathbf{w}_i$ [12]:

$$\mathbf{w}^L_{i+\frac{1}{2}} = \mathbf{w}_i - \frac{1}{2}\varphi^L_{i+\frac{1}{2}}(\mathbf{w}_i - \mathbf{w}_{i-1}), \quad \mathbf{w}^R_{i+\frac{1}{2}} = \mathbf{w}_{i+1} - \frac{1}{2}\varphi^R_{i+\frac{1}{2}}(\mathbf{w}_{i+1} - \mathbf{w}_{i+2}), \tag{12}$$

with L and R the left and right side of cell face $i+1/2$, respectively. We apply a limiter function to each of the primitive variables individually. In the next step the Riemann problem is solved for the limited variables to obtain the flux:

$$\mathbf{F}_{i+\frac{1}{2}} = \mathbf{F}_{i+\frac{1}{2}}(\mathbf{q}(\mathbf{w}^L_{i+\frac{1}{2}}), \mathbf{q}(\mathbf{w}^R_{i+\frac{1}{2}})). \tag{13}$$

The limiter has the function of blending a higher-order method of our own choice, for smooth regions of the solution, and the first-order method, for regions with steep gradients. It is defined as a function of the adjacent slopes of each of the individual primitive variables:

$$\varphi^L_{i+\frac{1}{2}} = \varphi(\mathbf{r}^L_{i+\frac{1}{2}}), \ \varphi^R_{i+\frac{1}{2}} = \varphi(\mathbf{r}^R_{i+\frac{1}{2}}), \ \text{with} \ \ \mathbf{r}^L_{i+\frac{1}{2}} = \frac{\mathbf{w}_{i+1} - \mathbf{w}_i}{\mathbf{w}_i - \mathbf{w}_{i-1}}, \ \mathbf{r}^R_{i+\frac{1}{2}} = \frac{\mathbf{w}_i - \mathbf{w}_{i+1}}{\mathbf{w}_{i+1} - \mathbf{w}_{i+2}}. \tag{14}$$

Spekreijse [16] outlined sufficient conditions for the limiter to ensure preserving of monotonicity of the method. They can be put in the form:

$$m \leq \varphi(r) \leq M, \quad -M \leq \frac{\varphi(r)}{r} \leq 2 + m, \quad \forall r \in \mathbb{R}. \tag{15}$$

The choice of the parameter M, if chosen to be greater than 1, causes a time-step restriction. In order for the method to be second-order accurate, $\varphi(1) = 1$ must hold and φ must be two times continuously differentiable around $r = 1$ [16]. Considering (15), this means $m \in [-1, 0]$. A new property we highlight here is a good handling of negative values of r, especially around $r = -1$, which corresponds to extrema. Often, the parameters in the monotonicity condition of Spekreijse are chosen to be $m = 0$ and $M = 2$. This leads to a region in the r, φ-plane, called the Sweby TVD (total variation diminishing) region [17]. A well-known class of schemes is formed by the van Leer κ-schemes [12], which correspond to $\varphi(r) = \frac{1-\kappa}{2} + \frac{1+\kappa}{2}r$, $\kappa \in [-1, 1]$. They are second-order accurate, and for $\kappa = \frac{1}{3}$ third-order accurate, but not monotone. The Koren limiter [10] follows the $\kappa = \frac{1}{3}$-scheme as much as possible inside the second-order Sweby region. It reads:

$$\varphi(r) = \begin{cases} 0, & r \leq 0, \\ \min\left(2r, \min\left(\frac{1}{3} + \frac{2}{3}r, 2\right)\right), & r > 0. \end{cases} \tag{16}$$

Here we propose an extended $\kappa = \frac{1}{3}$-limiter, which for a range of negative r-values around $r = -1$ coincides with $\kappa = \frac{1}{3}$ as well:

$$\varphi(r) = \begin{cases} \min(0, \max(-\frac{2}{3}, \frac{1}{3} + \frac{2}{3}r)), & r \leq 0, \\ \min(\frac{4}{3}r, \min(\frac{1}{3} + \frac{2}{3}r, 2)), & r > 0. \end{cases} \tag{17}$$

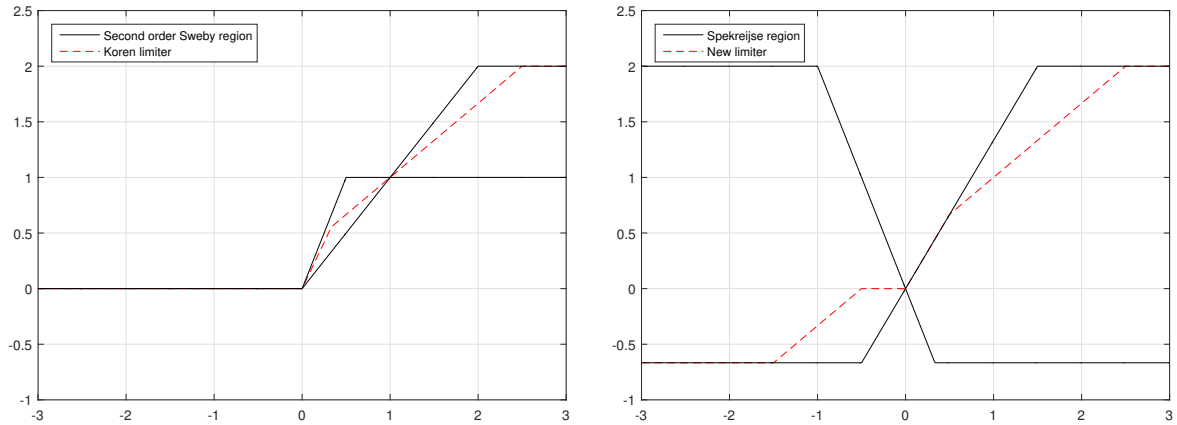

Figure 1: The limiters $\varphi(r)$ considered herein. On the left we see the Koren limiter inside the second-order Sweby region, on the right the new limiter, inside the Spekreijse region for $M = 2$ and $m = -\frac{2}{3}$.

To illustrate the effect of limiters, we compare them for the linear advection equation in one dimension, with two initial conditions, a discontinuous one and an infinitely smooth one. The initial solutions move undistorted at a constant velocity. The domain has periodic boundary conditions, so the exact solution after an integer number of periods is equal to the initial solution. We numerically calculate with 80 finite volumes, and we see that all limiters result in a positive, but much sharper resolution of the traveling discontinuities than the first-order upwind method. The minmod limiter, i.e., the lower bound of the second-order Sweby region is the most diffusive, as can be clearly seen in Figure 2. The superbee limiter, i.e., the upper bound of the second-order Sweby region is the most accurate. However, it may give false steepening of smooth profiles, as can also be seen in Figure 2. The Koren limiter and the new limiter are in between these two extremes.

3.2 HLLC Riemann solver

To compute the fluxes, instead of an exact Riemann solver, we apply an approximate Riemann solver, the HLLC scheme. We present this method for the x-direction, the y-direction is treated analogously.

The HLLC scheme assumes four regions of constant states separated by three discontinuous waves. The variables in the middle two regions are denoted with a superscript *. The outer two states are taken as the limited primitive variables on either side of the cell face

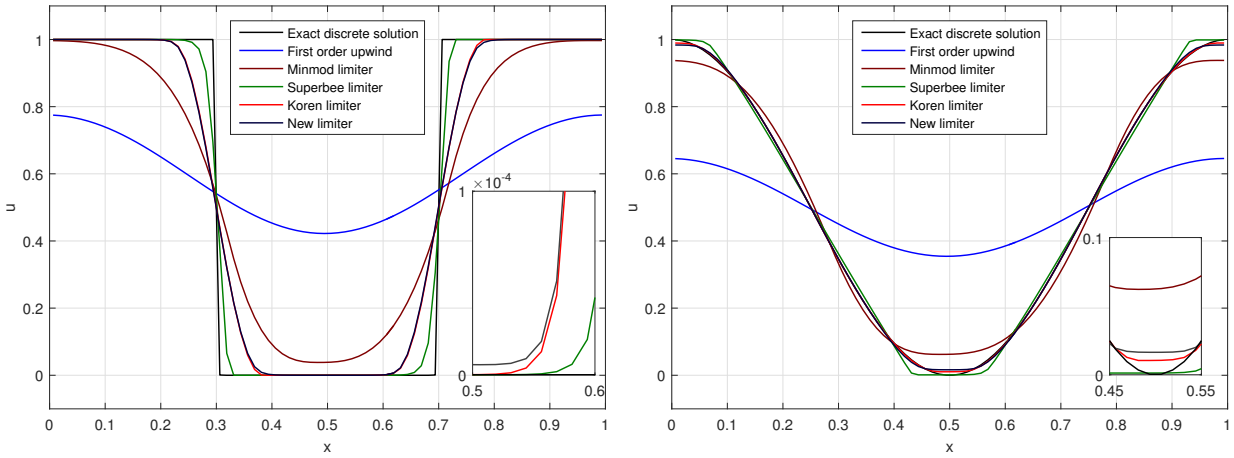

Figure 2: Comparison of various limiters and their effect on the linear advection, over 5 periods, of a discontinuous (left) and an infinitely smooth (right) initial condition.

considered. We denote them with subscripts L and R. We will work with the following estimates for the wave speed of the three wave fronts [3, 19]:

$$S_L = \min(u_L - c_L, (u-c)^{\text{Roe}}), \quad S_R = \max(u_R + c_R, (u+c)^{\text{Roe}}), \tag{18}$$

$$S_M = \frac{p_R - p_L + \rho_L u_L(S_L - u_L) - \rho_R u_R(S_R - u_R)}{\rho_L(S_L - u_L) - \rho_R(S_R - u_R)}. \tag{19}$$

Here, the superscript Roe denotes Roe averaging, which is defined through the density, velocity and enthalpy ($H := E + \frac{p}{\rho}$):

$$\rho^{\text{Roe}} = \sqrt{\rho_L \rho_R}, \quad u^{\text{Roe}} = \frac{\sqrt{\rho_R}u_R + \sqrt{\rho_L}u_L}{\sqrt{\rho_R} + \sqrt{\rho_L}}, \quad H^{\text{Roe}} = \frac{\sqrt{\rho_R}H_R + \sqrt{\rho_L}H_L}{\sqrt{\rho_R} + \sqrt{\rho_L}}. \tag{20}$$

Furthermore, following the model's underlying assumptions, we impose

$$u_L^* = u_R^* = S_M, \quad p_L^* = p_R^* = p^*. \tag{21}$$

To obtain $\mathbf{q}_L^*$ and $\mathbf{q}_R^*$ we solve the Rankine-Hugoniot conditions:

$$S_K \mathbf{q}_K^* - \mathbf{f}(\mathbf{q}_K^*) = S_K \mathbf{q}_K - \mathbf{f}(\mathbf{q}_K), \tag{22}$$

with $K = L, R$, across each wave front. Next we determine the flux at the cell interface ($x = 0$). We define four fluxes. The choice of the final flux is based on the direction of the wave speed estimates:

$$\mathbf{F} = \begin{cases} \mathbf{f}(\mathbf{q}_L), & S_L, S_M, S_R \geq 0, \\ \mathbf{f}(\mathbf{q}_L^*), & S_R, S_M \geq 0, S_L < 0, \\ \mathbf{f}(\mathbf{q}_R^*), & S_R \geq 0, S_L, S_M < 0, \\ \mathbf{f}(\mathbf{q}_R), & S_L, S_M, S_R < 0. \end{cases} \tag{23}$$

The flux $\mathbf{F}$ is calculated for every cell interface and complemented with fluxes at the edges of the domain resulting from the boundary conditions.

3.3 Non-conservative volume fraction term

The non-conservative term in (10), containing the right-hand side of the sixth equation of (3) is handled in an HLLC-type way, as proposed in [8]. In the x-direction this is done by:

$$S_i^n = (\alpha_i - \phi_i)\,(u_{i+\frac{1}{2}} - u_{i-\frac{1}{2}}),\ u = \begin{cases} u_L, & S_L, S_M, S_R \geq 0, \\ S_M, & S_R \geq 0, S_L < 0, \\ u_R, & S_L, S_M, S_R < 0. \end{cases} \tag{24}$$

The y-direction is handled analogously.

3.4 Time integration

We implement an explicit third-order accurate Runge-Kutta method with Butcher tableau [7]:

$$\begin{array}{c|ccc} 0 & & & \\ 1 & 1 & & \\ \frac{1}{2} & \frac{1}{4} & \frac{1}{4} & \\ \hline & \frac{1}{6} & \frac{1}{6} & \frac{2}{3} \end{array} \tag{25}$$

This time integrator was studied in [15], where it was shown to be a *TVD Runge-Kutta method* [13], meaning that the TVD property of the explicit Euler method extends to this time integrator.

3.5 Initial and boundary conditions

In the following, two types of boundary conditions will be considered: one representing a solid wall and the other a free outflow. The numerical implementation of this is done by adding virtual cells around the edges of the domain. Then, a (trivial) Riemann problem is solved, as is done in the interior cells, to determine the fluxes and the non-conservative term.

In the case of an outflow boundary condition, the state in the virtual cell is copied from the adjacent cell.

The solid wall is modeled by reflection; the state in the adjacent cell is copied, with the exception of the velocity component normal to the cell boundary, which changes sign. This results in a trivial Riemann problem, with either two identical shock waves or two identical rarefaction waves. The propagation velocity of the middle wave is zero. The only nonzero flux is in the momentum equation, due to the pressure.

In order to preserve strict positivity of the volume fraction, including round-off effects, we need to take a precaution in the initial condition for the volume fraction. In regions where a pure fluid is present, we take the values of α not to be 0 and 1, but ε and $1-\varepsilon$, for some small value of ε, 10^{-10} herein, representative for round-off.

3.6 Inertial forces

In the next section we will consider a liquid piston, accelerated by gravity g. This is modeled by adding a source term to the model (3) (in one spatial dimension):

$$\frac{\partial}{\partial t}\mathbf{q} + \frac{\partial}{\partial x}\mathbf{f} = \mathbf{s} + \mathbf{s}_g, \ \mathbf{s}_g = \left[0, \ \rho g, \ \rho g u, \ 0, \ 0\right]^T. \tag{26}$$

In numerical calculations of $\mathbf{s}_g$ we naturally take the cell averages of ρ and u.

4 Extended Bagnold model

In the original work of Bagnold [2] wave impacts are modeled by a solid piston with an initial velocity, moving towards a wall, with an ideal gas trapped in between. The problem then depends on only two parameters: the adiabatic constant of the gas γ_g and the dimensionless *Bagnold number* S_B. We consider a generalized Bagnold model [4], which

Figure 3: Sketch of extended Bagnold model.

consists of a closed tube, containing a liquid in between two gas layers. The liquid piston is driven by a body force, for instance gravity. The situation illustrated in Figure 3 is simulated using the numerical scheme outlined in the preceding section. This is done using 150 finite volumes and a CFL number of 0.49. The process is considered to be adiabatic and reversible. An exact solution can be found [4, 18] if the liquid is considered to be incompressible. In the model, the situation is completely described by five dimensionless numbers: length aspect ratio $\frac{L_0}{h_0}$, density ratio $\frac{\rho_g^0}{\rho_l^0}$, impact number $\frac{\rho_l^0 g L_0}{p_0}$, liquid compressibility $\frac{p_0}{\rho_l^0 \left(c_l^0\right)^2}$ and adiabatic constant of the gas γ_g in the perfect gas EOS (5), where the index 0 refers to the initial conditions.

The model is scaled in such a way that these dimensionless quantities remain the same. Brosset et al. [4] discuss this model in detail. We compare the numerical results for a number of benchmark cases [5] and we plot the pressures in Figure 4. The pressures of the two-fluid flow model and the piston-gas model [4] in Figure 4 coincide exactly. Furthermore there is complete similarity of cases 1 and 5. The piston-gas model assumes an incompressible liquid, whereas in the two-fluid flow model it is compressible. The difference is clearly seen in Figure 5 when increasing the impact number (through g). The compressibility of the liquid clearly softens the impact.

5 Shock-bubble interaction

Haas and Sturtevant [6] performed experiments with a cylindrical bubble, contained within a very thin nitrocellulose film, filled with a gas, being hit by a shock wave. We consider the

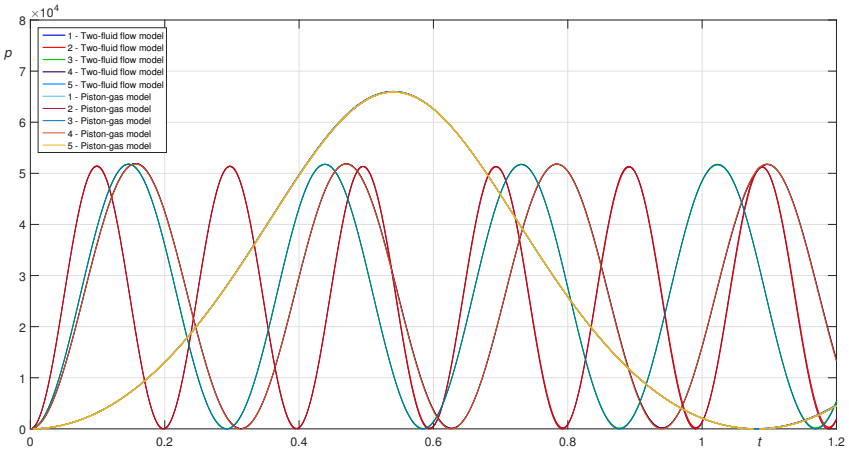

Figure 4: Comparison of the two-fluid flow model and the piston-gas model for the five test cases from [5].

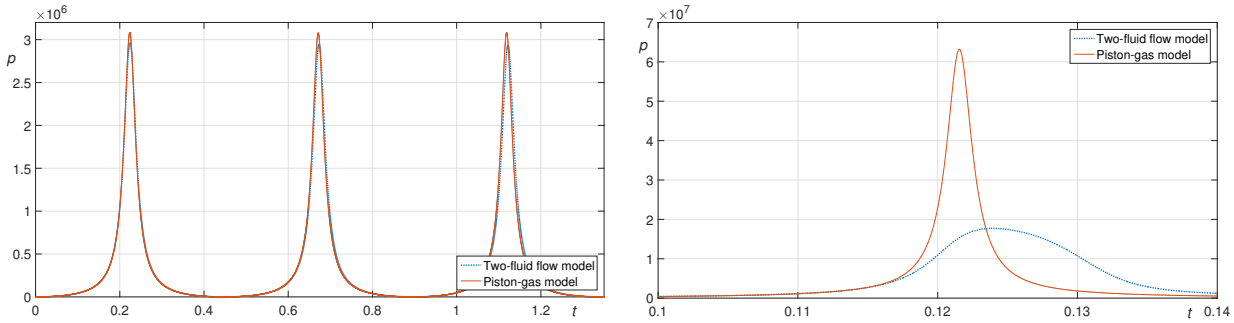

(a) $10g$ (b) $30g$

Figure 5: Comparison of the two-fluid flow model and the Bagnold model with increased impact numbers.

case in which the bubble is filled with of a heavier gas than the surrounding air. The experiment produced a number of shadow photographs which clearly show what happens to the bubble. This has become a benchmark for numerical simulation of compressible two-fluid flows [14, 11]. We numerically simulate the situation on a 356×960 rectangular grid with a CFL number of 0.24. The new limiter is used. Numerical tests have shown that this allows us to take the value of ε introduced in Section 3.5 to be 10^{-10}, whereas the other limiters require a value of $\varepsilon = 10^{-5}$ in order to preserve positivity.

The symmetry in the y-direction is utilized to simulate only half of the domain. For the case of a heavy gas in the bubble, R22, the bubble acts as a convergent optical lens. It gets compressed, and later, due to the velocity difference across its interface, instabilities arise. This is also seen in the results of the numerical simulation.

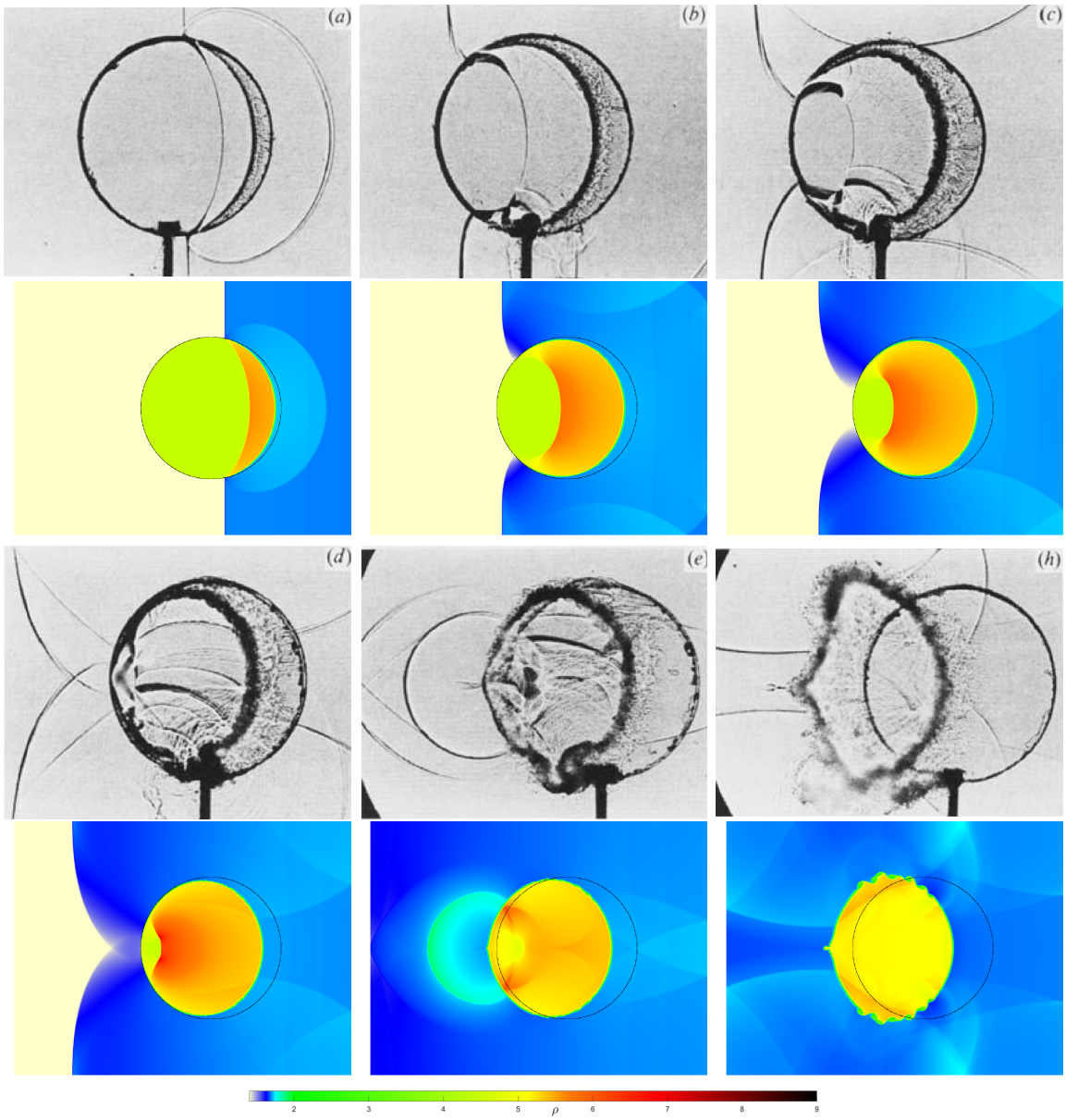

Figure 6: Results for the Haas-Sturtevant test case. Top: shadow photographs of the experiment, bottom: corresponding bulk density distributions from the numerical simulation.

6 Conclusion

In order to numerically simulate two-fluid flows, a novel numerical scheme has been developed for the quasi-conservative five-equation Kapila model. The HLLC approximate Riemann solver is applied to the conservative equations, whereas the non-conservative term is handled in an HLLC-type way. Spatial reconstruction is applied to achieve higher-order accuracy. This requires a limiter function, for which we introduce a new version. The nu-

merical method is applied to liquid impact on a gas pocket, and is tested for interaction of a shock wave with a bubble, showing its potency to handle both types of problems. The newly introduced limiter proves to be better than its alternatives at preserving positivity at high accuracy.

Acknowledgement

This work is part of the research programme SLING with project number P14-10.1, which is (partly) financed by the Netherlands Organisation for Scientific Research (NWO).

REFERENCES

[1] M.R. Baer and J.W. Nunziato. A two-phase mixture theory for the deflagration-to-detonation transition (DDT) in reactive granular materials. *International Journal of Multiphase Flow*, 12, pp. 861–889, 1986.

[2] R.A. Bagnold. Interim report on wave-pressure research. *Journal of the Institute of Civil Engineers*, 12, pp. 202–226, 1939.

[3] P. Batten, N. Clarke, C. Lambert, and D.M. Causon. On the choice of wavespeeds for the HLLC Riemann solver. *SIAM Journal on Scientific Computing*, 18, pp. 1553–1570, 1997.

[4] L. Brosset, J-M. Ghidaglia, P-M. Guilcher, and L. Le Tarnec. Generalized Bagnold model. *Proc. 23th Int. Offshore Polar Eng. Conf., Anchorage, Alaska, USA, ISOPE, Vol* 3, pp. 209-223, 2013.

[5] F. Dias and L. Brosset. Comparative numerical study: description of the calculation cases. *Proc. 20th Int. Offshore Polar Eng. Conf., Beijing, China, ISOPE, Vol* 33, 2010.

[6] J.F. Haas and B. Sturtevant. Interaction of weak shock waves with cylindrical and spherical gas inhomogeneities. *Journal of Fluid Mechanics*, 81, pp. 41-76, 1987.

[7] W. Hundsdorfer, B. Koren, M. van Loon, and J.G. Verwer. A positive finite-difference advection scheme. *Journal of Computational Physics*, 117, pp. 35–46, 1995.

[8] E. Johnsen and T. Colonius. Implementation of WENO schemes in compressible multicomponent flow problems. *Journal of Computational Physics*, 219, pp. 715–732, 2006.

[9] A.K. Kapila, R. Menikoff, J.B. Bdzil, S.F. Son, and D.S. Stewart. Two-phase modeling of deflagration-to-detonation transition in granular materials: Reduced equations. *Physics of Fluids*, 13, pp. 3002–3024, 2001.

[10] B. Koren. A robust upwind discretization method for advection, diffusion and source terms. Chapter 5 in *Notes on Numerical Fluid Mechanics*, 45. Vieweg, 1993.

[11] J.J. Kreeft and B. Koren. A new formulation of Kapila's five-equation model for compressible two-fluid flow, and its numerical treatment. *Journal of Computational Physics*, 229, pp. 6220–6242, 2010.

[12] B. Van Leer. Towards the ultimate conservative difference scheme V. A second-order sequel to Godunov's method. *Journal of Computational Physics*, 32, pp. 101-136, 1979.

[13] R. LeVeque. *Finite-Volume Methods for Hyperbolic Problems*. Cambridge University Press, 2002.

[14] S. Quirk and J. Karni. On the dynamics of shock-bubble interaction. *Journal of Fluid Mechanics*, 318, 1996.

[15] C. Shu and S. Osher. Efficient implementation of essentially non-oscillatory shock-capturing schemes. *Journal of Computational Physics*, 77, pp. 439–471, 1988.

[16] S. Spekreijse. Second-order discretization of hyperbolic conservation laws. *Mathematics of Computation*, 49, pp. 135–155, 1987.

[17] P.K. Sweby. High resolution schemes using flux limiters for hyperbolic conservation laws. *SIAM Journal on Numerical Analysis*, 21, pp. 995–1011, 1984.

[18] A.S. Tijsseling, Q. Hou, and Z. Bozkuş. Analytical solutions for liquid slugs and pigs traveling in pipelines with entrapped gas. *Proc. ASME Pres. Ves. and Pip. Conf., Waikoloa, Hawaii, USA, PVP Vol 4*, 2017.

[19] E.F. Toro. *Riemann Solvers and Numerical Methods for Fluid Dynamics*. Springer, 2009.

[20] J. Wackers and B. Koren. A fully conservative model for compressible two-fluid flow. *International Journal for Numerical Methods in Fluids*, 47, pp. 1337–1343, 2005.

[21] A.B. Wood. *A Textbook of Sound*. Bell, 1964.